Full length article

Crystal growth during keyhole mode laser welding

H.L. Wei [a], J.W. Elmer [b], T. DebRoy [a, *]

[a] Department of Materials Science and Engineering, The Pennsylvania State University, University Park, PA 16802, USA
[b] Materials Engineering Division, Lawrence Livermore National Laboratory, Livermore, CA 94550, USA

ARTICLE INFO

ABSTRACT

Evolution of microstructure during keyhole mode welding involves several special features such as multiple inflections of weld pool boundary curvatures, strong spatially variable thermal cycles and negligible undercooling. These systems are difficult to characterize rigorously, because depending on the sections selected, significantly different grain structures and topological features are observed. Here we uncover the special features of crystal growth during keyhole mode laser welding considering the motion of the melt pool and the interdependence of the grain growth in both the fusion zone and the heat affected zone. The temperature distribution and the transient thermal history of welds were combined with the grain growth simulation using a Monte Carlo approach in a computationally efficient manner. The computed results were tested against independent experimental data for keyhole mode laser welding of copper where the grain structure can be easily resolved. The results showed that the curved columnar grains growing from the fusion zone boundary coexisted with axial columnar grains near the centerline of welds. The effects of welding speed on the dimension, distribution, orientation and morphology of the columnar and equiaxed grains were studied.

1. Introduction

Keyhole mode laser welding is widely used to join large components of many important engineering alloys. Due to very high energy density of the laser beam, a vapor cavity known as the keyhole forms inside the components surrounded by a pool of liquid metal which solidifies to form the weld as the laser beam moves along [1,2]. Evolution of microstructure during keyhole mode welding is characterized by several special features that are very different from most fusion welding processes including conduction mode laser welding where the power density is insufficient to form a keyhole [3,4]. They include very high peak temperature close to the boiling temperature of the alloy, a moving solidification front with multiple inflection points, strong spatial variations of thermal cycles, and negligible constitutional and kinetic undercooling, all of which affect microstructure evolution in a manner unlike any other fusion welding process [5–7].

The grain structure evolution during keyhole mode welding is significantly different from that in conduction mode laser welding or gas tungsten arc welding and most previous studies were focused on welds that did not form any keyhole. For example, grain structure evolution within the heat affected zone (HAZ) was simulated based on a Monte Carlo (MC) technique [8–11]. Computationally intensive cellular automaton model was used to simulate the 3D grain growth in the fusion zone (FZ) while ignoring grain growth in the HAZ [12–14]. Grain structure prediction in an aluminum alloy weld was reported based on a MC technique considering the temporal and spatial distributions of temperature field during gas tungsten arc welding [15]. However, studies of grain growth during keyhole mode laser welding are scarce.

Grain growth in keyhole mode welds is difficult to characterize rigorously, because depending on the sections selected, significantly different grain structures and topological features are observed because of the multiple inflections of weld pool boundary curvatures and other complexities [3,16]. By incorporating a well known fact that directions of grain growth are normal to the weld pool boundary [17], and these directions may be different from the directions of growths of cells and dendrites, crystal growth and topological features can be rigorously probed for keyhole mode welding. Simulation of the grain structure evolution requires reliable three dimensional (3D) transient temperature fields [1,18,19]. In addition, both the moving liquid pool and the interdependent grain growth in the FZ and the HAZ need to be considered to reveal the grain growth process.

* Corresponding author.
E-mail address: rtd1@psu.edu (T. DebRoy).

A highly localized solidification structure in the FZ is generated behind the moving melt pool during welding. The solidified grain structure is affected by both the temperature field near the solidification front and the grain morphology and orientation in the HAZ [20]. Grains at the solidification front in the FZ initially grow epitaxially with the partially melted grains in the HAZ. The subsequent growth depends on the preferred crystallographic orientation of the solidification structure as well as the local temperature gradient at the solidification front [21]. During keyhole mode laser welding, straight axial columnar grains growing along the welding direction are observed near the centerline of the FZ, coexisting with curved columnar grains growing from the fusion line [3]. In order to better understand the grain growth process during keyhole mode welding, it is essential to model the evolution of columnar and equiaxed grains in both the FZ and the HAZ.

Here we report the evolution of columnar grains in the FZ and the equiaxed grains in the HAZ in three dimensions considering their interdependence during keyhole mode laser welding of copper. Both the temporal evolution and the spatial distribution of the grain structure were simulated by a 3D grain growth model. The effects of the welding speed on the orientation, morphology, dimension and distribution of the columnar and equiaxed grains were studied. The simulated results from the model are tested against independent experimental data.

2. Models and methodology

2.1. heat transfer and fluid flow model

The temperature and velocity fields during keyhole mode laser welding of copper are computed using a 3D heat transfer and fluid model. The details of the governing equations, boundary conditions and the algorithm can be found in our previous papers [18,22,23]. The composition of the copper, the data used for the calculation and the welding process parameters are presented in Tables 1–3, respectively.

2.2. Grain growth model

2.2.1. Assumptions

(1) The shape and the size of the weld pool are constant during the welding process. The validity of this assumption can be recognized in the reported results [3].
(2) The grain growth direction is parallel to the maximum heat flow direction which is normal to the boundary of the weld pool [17].
(3) The formation of the subgrain structure is not considered because it does not have significant effect on the macroscopic grain structure for polycrystalline materials [17].
(4) Solute redistribution and microsegregation during solidification are not considered because nearly pure copper (99.9% Cu) was used in this work.
(5) Undercooling during solidification is not considered because it is small under the conditions examined in this paper. Constitutional undercooling which is significant during welding of alloys can be neglected here because the material used in this study was nearly pure copper. As a result, it is fair

Table 1
Chemical compositions of the copper used in this work (wt. %) [3].

Cu	Fe	S	Pb	As	Sb	Bi	O
≥99.9	≤0.005	≤0.005	≤0.005	≤0.002	≤0.002	≤0.001	≤0.06

Table 2
Data used for the calculation of temperature and velocity fields [34].

Variables	Value
Laser beam radius (mm)	0.1
Laser absorptivity	0.13
Solidus temperature (K)	1338
Liquidus temperature (K)	1356
Boiling temperature (K)	2835
Density of liquid metal (kg m^{-3})	8.02
Thermal conductivity of solid (W m^{-1} K^{-1})	330
Thermal conductivity of liquid (W m^{-1} K^{-1})	163
Viscosity of liquid (kg m^{-1} s^{-1})	0.004
Temperature coefficient of surface tension (N m^{-1} K^{-1})	−0.23
Specific heat of solid (J g^{-1} K^{-1})	0.47
Specific heat of liquid (J g^{-1} K^{-1})	0.49
Coefficient of thermal expansion (K^{-1})	1.66×10^{-5}

Table 3
Laser welding process parameters [3].

Weld No.	Welding speed (m/min)	Laser power (kW)	Plate thickness (mm)
1	1.0	4.0	1.5
2	7.0	4.0	1.5
3	8.0	4.0	1.5

to assume that the solidification front is located on the solidus isotherm of the weld pool.

(6) Recrystallization in the copper plate is not considered. The work focuses on the grain growth in the FZ and the HAZ under the influence of various thermal cycles.

2.2.2. Grain growth in the HAZ

The grain growth in the HAZ is simulated using MC technique which is based on the Potts' model [24]. The details of the model are available in the literature [8,10,15,25,26] and the salient features are presented in Appendix A1.1. A relation between the MC simulation time and real time was established through a grain boundary migration model, considering the material properties and temperature time history in the grain growth kinetics [15,27]. The site selection probability is calculated according to the intensities of the thermal cycles experienced by each site. Locations with higher MC simulation time have higher site probability and are updated more frequently. Therefore, grains grow faster in regions that experience stronger thermal cycles which is determined by the area under the temperature versus time plot. The data used for grain growth calculation are presented in Table 4.

2.2.3. Grain growth in the FZ

Columnar grains in the FZ grow epitaxially from the partially

Table 4
Data used for grain growth calculation by MC simulation [3,32].

Variables	Value
Initial grid spacing (μm), L_0	15
Grain boundary energy (J m^{-2}), γ	0.625
Accommodation probability, A	1.0
Average number per unit area at grain boundary (atoms m^{-2}), Z	2.0×10^{19}
Activation enthalpy for grain growth (J mol^{-1}), Q	9.34×10^4
Atomic molar volume (m^3 mol^{-1}), V_m	7.11×10^{-6}
Avagadro's number (mol^{-1}), N_a	6.02×10^{23}
Planck's constant (J s), h	6.624×10^{-34}
Activation entropy (J mol^{-1} K^{-1}), ΔS_a	9.48
Gas constant (J K^{-1} mol^{-1}), R	8.314

melted grains in the HAZ at the solidification front. Subsequently the columnar grains grow along location dependent directions and rates. The details of the calculation of the local growth direction and rate on the solidifying surface of the weld pool can be found in our previous papers [15,20,28] and the salient features are presented in Appendix A1.2. The freshly solidified grains in the FZ thicken in size which is simulated using the MC model.

At steady state, the motion of the weld pool determines the solidification growth rate which depends only on the welding speed. In other words, the movement of the solidus line with time determines the position on the growth interface. The direction of grain growth is influenced by the maximum heat flow direction and this direction aligns closely with ⟨100⟩ for face-centered cubic materials such as copper in most cases. In other words, growth occurs perpendicular to the boundary of the melt pool. At high solidification growth rates, the growth direction may deviate from the heat flow direction. Experimental data on the extent of misalignment between the maximum heat flow direction and the crystal growth direction are not available for the laser processing of copper and has been neglected in the current investigation. The local growth direction is modified after each incremental movement of the weld pool depending on the 3D temperature gradients which affects the local curvature of the solidus surface.

2.2.4. Numerical scheme

The 3D simulations were conducted in a cubic lattice system. The computational domain included only one half of the specimen due to the symmetry of the weld. In the 3D grain growth model the grid spacing is 15 μm in x-, y- and z-directions, which is equal to the initial base metal grain size. The variation of grid spacing does not affect the final grain structure significantly because the effect of grid spacing on the grain size has already been considered in the MC simulation algorithm. Non-uniform coarser grids were used in the heat transfer and fluid flow model to calculate the temperature field, which was subsequently interploted in the grain growth model.

2.3. Calculation procedure

(1) The temperature field is calculated from the keyhole model laser welding heat transfer and fluid flow model, which is then read as the input data for the grain growth model.
(2) The computational domain for grain growth is initialized.
(3) The melt pool progresses one step and the temperature field is updated.
(4) The computational domain is scanned to detect the boundary of the melt pool.
(5) The grains in the FZ epitaxially grow from the grains in the HAZ and the FZ.
(6) The MC technique is applied to the grains in both the HAZ as well as the FZ.
(7) Steps 3 to 6 are repeated until the calculation has been completed.

3. Results and discussion

3.1. Temperature field, liquid metal flow and weld geometry

The calculated 3D temperature and velocity fields during keyhole mode laser welding of copper are shown in Fig. 1 (a), (b) and (c) for welding speeds of 1.0, 7.0 and 8.0 m/min, respectively. The molten metal flows from the keyhole to the periphery of the weld pool on the top surface. The main driving force is the Marangoni stress that results from the spatial variation of surface tension. The flow velocities are of the order of 100 mm/s, which indicates that convective heat transfer is significant in the melt pool.

The heat transfer and fluid flow model is validated against experimental results [3] as shown in Fig. 2. The agreement in the shapes and dimensions of the welds indicates the accuracy of the computed temperature distributions, which are used to determine the maximum temperature gradients at the molten pool boundary. Note that the coordinate system used in Figs. 1 and 2 applies through the subsequent discussion of the results. The x-y planes are defined as horizontal planes, the x-z planes are longitudinal planes, and the y-z planes are transverse planes.
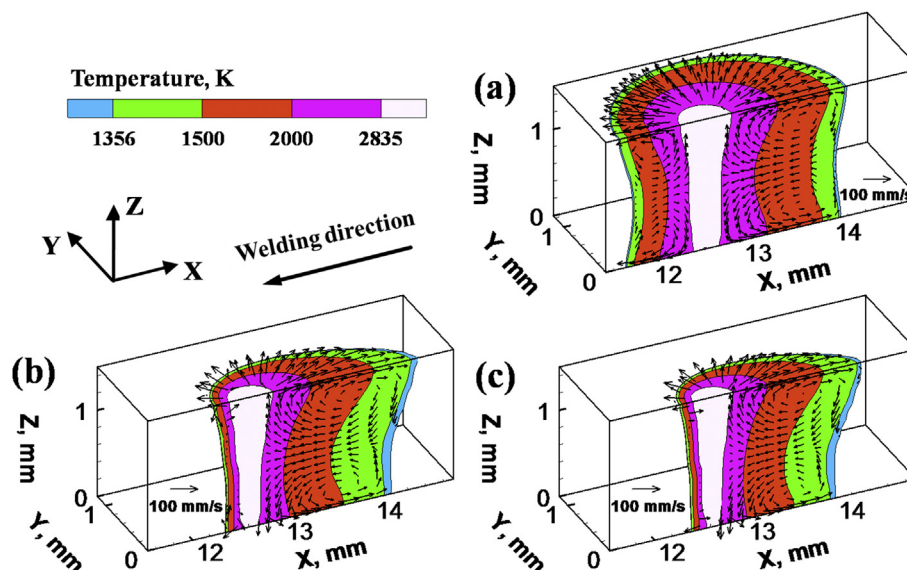

Fig. 1. Calculated temperature and velocity fields for various welding speeds. (a) 1 m/min, (b) 7 m/min, (c) 8 m/min.
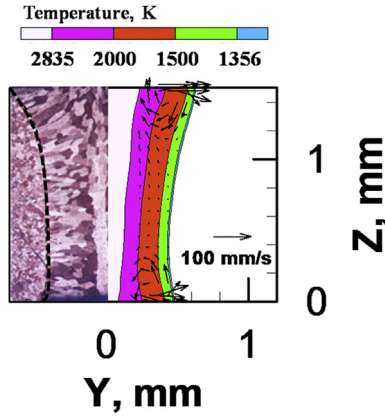
Fig. 2. Comparison of the experimentally observed transverse section [3] with that calculated by the 3D numerical model. Welding speed: 7 m/min.

3.2. Heat flow directions

The size of the molten pool decreases with increasing welding speed, as shown in Figs. 1 and 3. In addition, the shape of the pool varies with welding speed as well. The top surface of the pool is elliptical at a welding speed of 1.0 m/min. It is significantly elongated at welding speeds of 7.0 m/min and 8.0 m/min. The upper parts of the trailing edges of the pools are further inclined with greater welding speeds. Fig. 3 shows that such shape changes lead to significant variations of the maximum heat flow directions at the molten pool boundary, which will further result in different grain growth patterns during solidification.

3.3. Grain structure in the FZ and the HAZ

3.3.1. Temporal evolution of grain structure

The simulated grain growth results at welding speed of 7 m/min are taken as an example to illustrate the 3D evolution of the grain structures in both the FZ and the HAZ. Fig. 4 shows one set of horizontal and longitudinal cross sections of the weld at time increments of 0.01, 0.04, and 0.08 s after the start of welding. In this figure, the trailing edge of the molten pool on the x-axis is located at x = 12.2 mm at the starting position. As the welding direction is along the − x direction, the corresponding point moves to x = 11.0 mm after 0.01 s, x = 7.5 mm after 0.04 s, and x = 2.8 mm after 0.08 s of welding time with the welding speed of 7 m/min. The calculations reproduce the molten pool shape, and clearly show the FZ and HAZ grains.
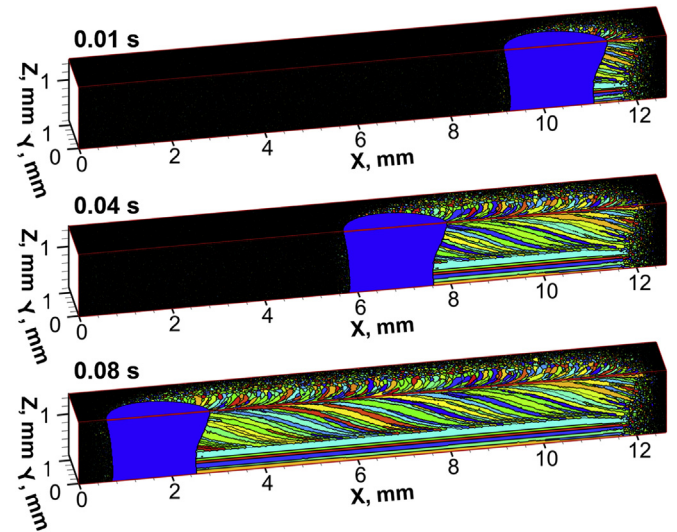

Fig. 4. Temporal evolution of the grain structure in the horizontal top and longitudinal central planes. Welding speed: 7 m/min.

During the movement of the molten pool, equiaxed grains in the HAZ continue to experience grain growth as they pass through the moving temperature gradient. Grains closest to the fusion line have the largest average size, and the size decreases with distance from the fusion line. In the meantime, solidification occurs in the FZ with the formation of columnar grains growing epitaxially from the partially melted grains in the HAZ at the fusion line. The simulated results in Fig. 4 show that the grain growth model is capable of predicting the temporal evolution of the grain structure in both the FZ and the HAZ with the time accuracy on the order of 0.01 s.

3.3.2. Grain structure in the transverse section

Fig. 5 shows the comparison of the simulated and the experimentally observed grain structure in both the FZ and the HAZ in the transverse cross section. It is shown in both Fig. 5 (a) and (b) that the FZ is occupied with columnar grains and the HAZ is composed of equiaxed grains. The orientations of the columnar grains are approximately horizontal in the lower half part of the FZ. However, the columnar grains grow with inclined angles in the upper half part of the FZ. The reason is that the fusion boundary is in a curved rather than straight shape, as shown in Fig. 2 (b). The lower part of the fusion boundary is almost vertical and the upper part is inclined gradually. The local maximum heat flow directions are perpendicular to the fusion boundary, which determines the growth
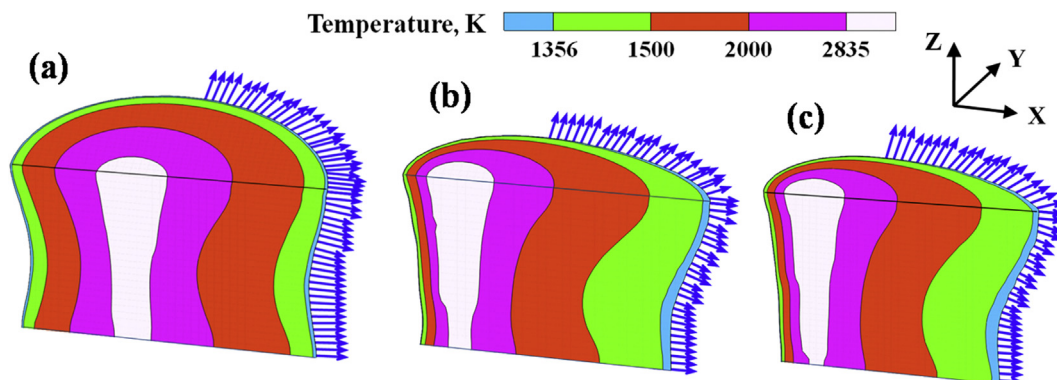

Fig. 3. Calculated 3D heat flow directions at the boundary of the weld pool with various welding speed. (a) 1 m/min, (b) 7 m/min, (c) 8 m/min.
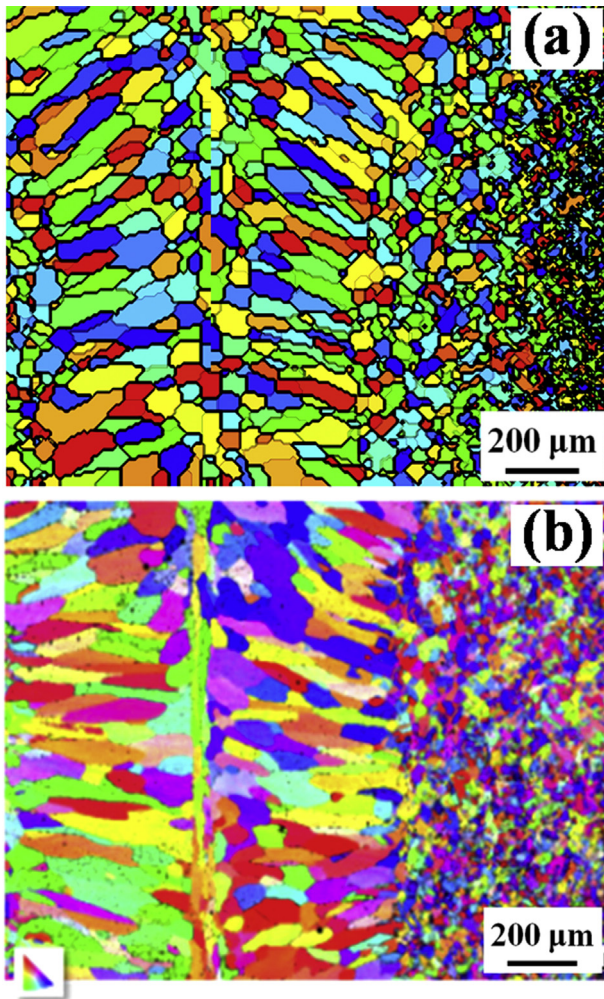
Fig. 5. Comparison of the grain structure in both the FZ and the HAZ in transverse y-z plane. (a) Simulated result from the 3D grain growth model, (b) experimentally observed result by EBSD [3]. Welding speed: 7 m/min.

directions of the columnar grains. The simulated grain growth results from the 3D grain growth model agree well with the grain structure revealed by EBSD characterization [3].

3.3.3. Grain structure in horizontal planes

Fig. 6 shows the comparison of the grain structure in the horizontal x-y planes of the FZ near the top and bottom surfaces. Both the simulated and experimentally characterized results demonstrate that the cross sections of the columnar grains have significantly different appearances. The columnar grains in the horizontal plane near the bottom surface of the weld show relatively complete shapes than those in the plane near the top surface. Note that elongated axial columnar grains can be observed in the middle of the FZ in Fig. 6 (c) and (d). However, such axial grains are absent in Fig. 6 (a) and (b). Instead, several discontinuous columnar grains with orientations parallel to the welding direction exist in the middle of the FZ. Apparently, the average length and aspect ratio of the columnar grains in the two horizontal x-y planes near the top and bottom surfaces are significantly different.

In order to understand the transition of the morphologies of the columnar grains in the horizontal x-y sectional planes along the z-direction, the average length and aspect ratio of the columnar grains in various horizontal planes are examined. Fig. 7 (a) shows the comparison of average length of the columnar grains in horizontal x-y planes from the top to the bottom surfaces of the weld with a distance step of 75 μm. The error bars indicate the effect of the random size and orientation of the HAZ equiaxed grains on epitaxial growth of columnar grains in the FZ. The maximum average length 460 μm appears on the bottom surface and the minimum average length 200 μm locates in the horizontal plane about 0.45 mm from the top surface. The average length is about 320 μm on the top surface, which is approximate to the average of the maximum and minimum values. Such variation of the average length of the columnar grains indicates the change of the average angles between the growth directions of the columnar grains and the horizontal planes in the 3D domain. The average angle initially increases between the bottom surface and the horizontal plane with distance 0.45 mm from the top surface. Then the angle decreases between this interior plane and the top surface.
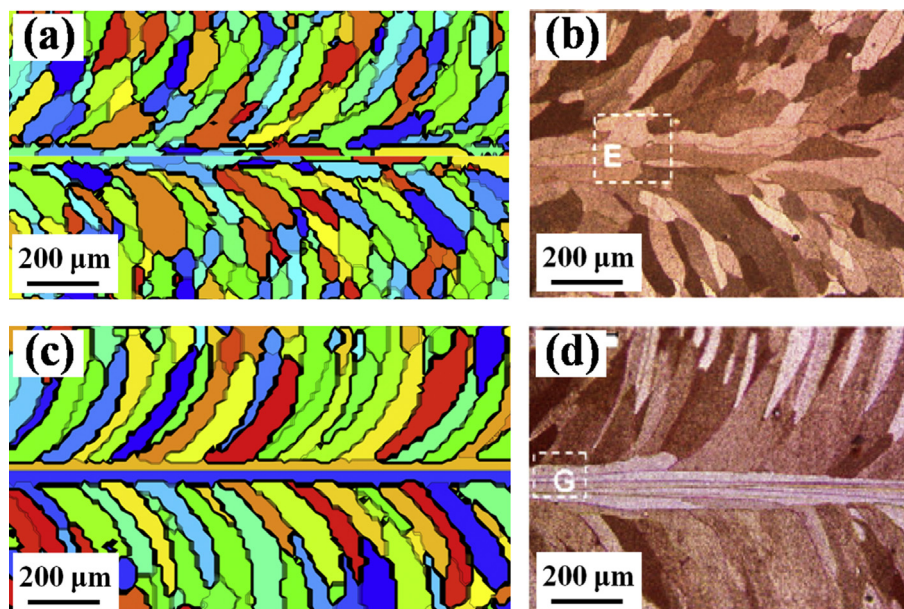

Fig. 6. Comparison of the grain structure in horizontal x-y planes of the FZ near the top and bottom surfaces. (a) 60 μm from the top surface; (c) 60 μm from the bottom surface. (a) and (c) are simulated results, (b) and (d) are experimentally observed results [3]. Welding speed: 7 m/min.
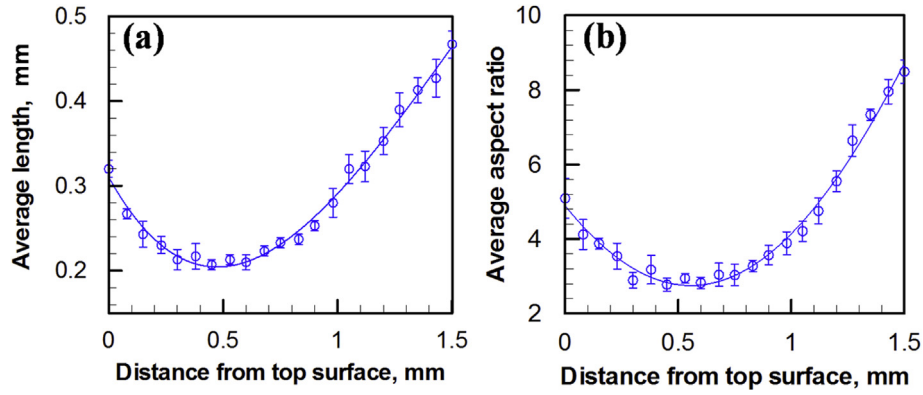
Fig. 7. Comparison of the average size and aspect ratio of the columnar grains in the horizontal x-y planes. Welding speed: 7 m/min.
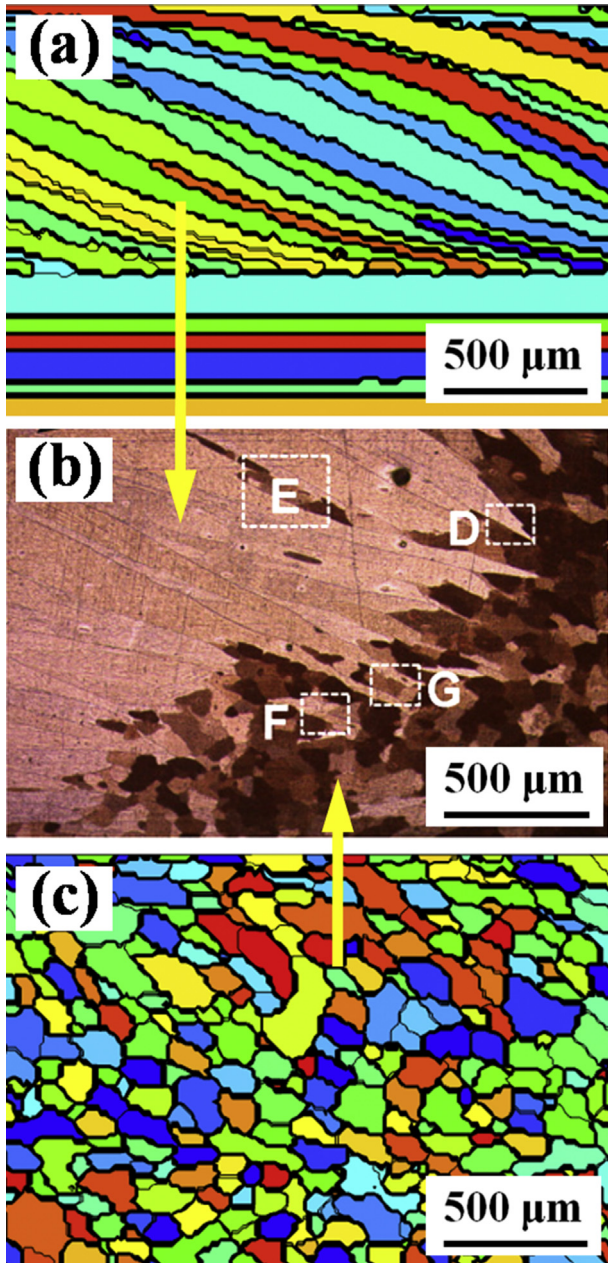

Fig. 8. Comparison of the grain structure in longitudinal x-z planes of the FZ. (a) Longitudinal central plane; (c) 150 μm from longitudinal central plane. (a) and (c) are simulated results, (b) is experimentally observed results [3]. Welding speed: 7 m/min.

The average aspect ratio of the columnar grains is shown in Fig. 7 (b), which has similar trend with the average length. The aspect ratio of a columnar grain is defined as the length divided by the thickness. Note that the individual axial columnar grains in the middle of the weld may have extremely large aspect ratio due to their comparable lengths with that of the entire weld. One main advantage of modeling over experimental characterization of grain structure is that the grain size and shape for the entire weld region along any arbitrary virtual cross section can be visualize and analyzed. For instance, it will be rather difficult to experimentally examine the variation of the average length and aspect ratio of the columnar grains in 21 consecutive horizontal planes within the thickness of 1.5 mm, which has been readily revealed by the 3D grain growth model.

3.3.4. Grain structure in longitudinal planes

Fig. 8 shows the comparison of the grain structure near two longitudinal planes of the FZ. The simulated grain structure is exactly from longitudinal x-z planes. But the experimentally observed grain structure was obtained from a vertical sectioning plane which was not parallel to the x-z plane. More details about the configuration of the experimental characterization can be found from the literature [3]. It can be observed from Fig. 8 (a) and the left hand part of Fig. 8 (b) that the longitudinal central x-z plane is composed of columnar grains. The orientations of these columnar grains are approximated horizontal in the lower part of the FZ. On the contrary, the columnar grains are inclined in the upper part of the FZ. The appearances of the grains are strikingly different in the longitudinal x-z plane with a distance of 150 μm from the central longitudinal plane, which are shown in Fig. 8 (c) and the right hand part of Fig. 8 (b). Note that only columnar grains form in the FZ during solidification [3]. Such dramatic change of the grain appearances in two adjacent longitudinal x-z planes originates from the coexistence of elongated axial columnar grains in the middle of the FZ growing along the welding direction and the curved columnar grains growing from the edge to the middle of the FZ. The grain structure revealed in the transverse and horizontal planes shown in Figs. 5 and 6 can help understanding the unique variation of grain appearances in the longitudinal planes.

The average length and aspect ratio of the columnar grains in various longitudinal planes are examined to understand the transition of the morphologies of the columnar grains along the y-direction. Fig. 9 (a) shows the comparison of average length of the columnar grains in longitudinal x-z planes from the middle to the edge of the FZ with a distance step of 30 μm. The maximum average length 1.2 mm appears in the central longitudinal plane and the minimum average length 130 μm locates in the longitudinal plane at the edge of the FZ. The average length drops drastically from the
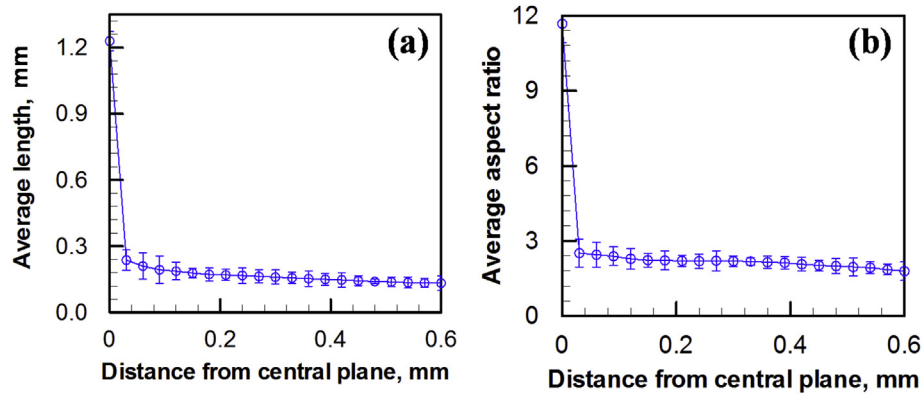
Fig. 9. Comparison of the average size and aspect ratio of the columnar grains in the longitudinal x-z planes. Welding speed: 7 m/min.

central to the interior longitudinal planes. The average aspect ratio of the columnar grains has similar trend of variation with distance from the central longitudinal plane, which is shown in Fig. 9 (b).

It was reported that failure often occurred in regions with straight axial columnar grains during the transverse tensile tests [29]. Welds containing axial columnar grains are also susceptible to centerline solidification cracking [17]. One reason is that near the weld centerline columnar grains transform from elongated straight to short curved shapes with nearly perpendicular growth directions. The steep angle favors the impingement of the columnar grains. In addition, residual tensile stresses exist in the weld metal and the adjacent base metal, while residual compressive stresses exist in the areas farther away from the weld metal [17]. Thus, fracture occurs more easily near the weld centerline under the influence of transverse tensile stresses.

3.3.5. Effect of scanning speed on grain structure evolution

The effect of welding speed on the grain structure in the horizontal x-y planes near the bottom of the welds is shown in Fig. 10. Both the simulated and experimentally observed results show that the grains are coarser at welding speed of 1 m/min over 8 m/min.

More interestingly and importantly, the width of the region composed of axial columnar grains is significantly larger at welding speed of 1 m/min. The heat flow directions in the region close to the middle of the FZ are approximately parallel to the welding direction, as shown in Fig. 3. The width of such region decreases with greater welding speed due to the change of weld pool shapes. Note that the growth directions of the columnar grains are dependent on the local maximum temperature gradients at the molten pool boundary. As a result, the width of the region with axial columnar grains is reduced from approximately 300 μm to 20 μm when the welding speed increases from 1 m/min to 8 m/min. Note that the grain growth modeling was done for half of the weld because of symmetry. The simulated grain structure shown in Figs. 5, 6 and 10 were obtained by both halves of the same weld.

Fig. 11 further shows the simulated 3D grain structure by constructing collectively the horizontal top plane, longitudinal central plane, and the corresponding transverse plane. The effect of heat input and the shape of the weld pool on the grain structure can be visualized directly. As shown in Fig. 11 (a), the growth directions of the columnar grains near the fusion boundary are mostly perpendicular to the fusion line in the horizontal x-y and transverse y-z
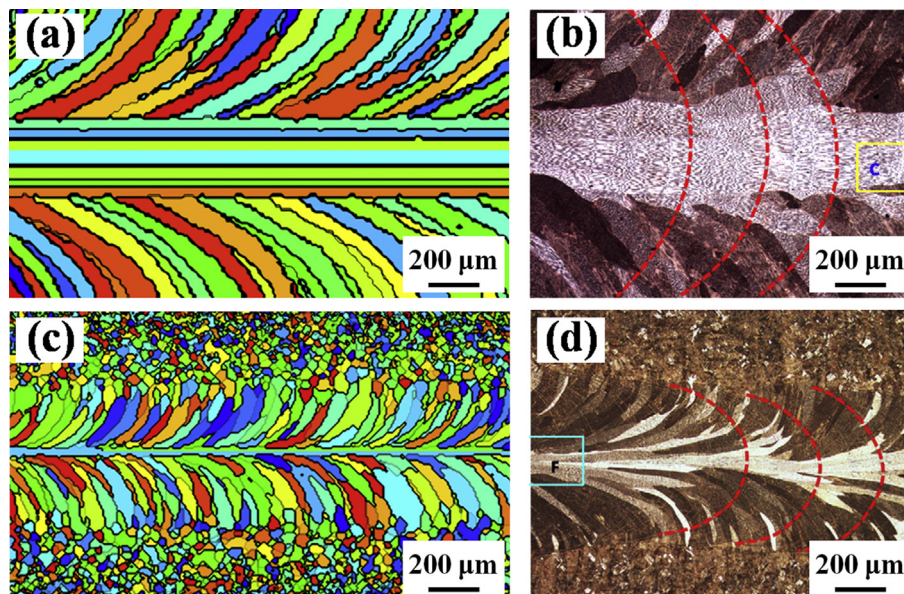

Fig. 10. Comparison of the grain structure in the horizontal x-y planes near the bottom of the welds. (a) and (b) welding speed of 1 m/min. (c) and (d) welding speed of 8 m/min. (a) and (c) are simulated results, (b) and (d) are experimentally observed results [3].
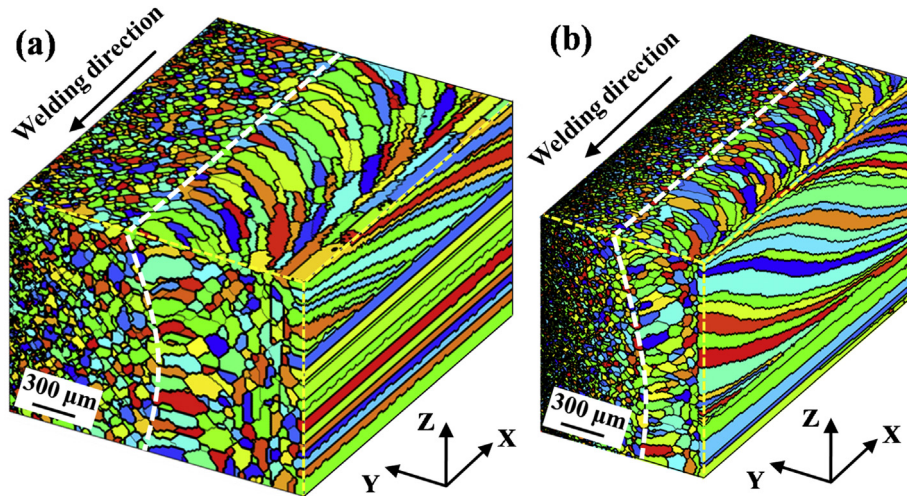
Fig. 11. Comparison of the simulated 3D grain structure for different welding speed in x-y, y-z, and x-z planes, respectively. (a) 1 m/min, (b) 8 m/min.

planes. The growth directions tend to be parallel to the welding direction in the region close to the centerline of the FZ. On the contrary, it can be observed from Fig. 11 (b) that the width of region with nearly parallel grain growth and welding directions decreases significantly. Furthermore, in the longitudinal central plane the height of the area composed of axial columnar grains decreases significantly when the welding speed increases from 1 m/min to 8 m/min. Note that in the transverse y-z plane the columnar grains near the centerline of the FZ have similar appearances to equiaxed grains, which might be misleading when observing the grain structure in transverse cross sections. Remarkably, such visualization of the 3D grain structure as shown in Fig. 11 can provide extensive details on the morphologies, orientations, dimensions, and distributions of grains in both the FZ and the HAZ.

Fig. 12 (a) shows the variation of average grain area in various horizontal x-y planes at welding speed of 1 m/min and 8 m/min. Similar to the change of average grain length in the horizontal planes at welding speed of 7 m/min, the average grain area initially decreases and then increases with greater distance from the top surface of the FZ. However, the location from the top surface where the minimum average grain area appears increases from about 0.2 mm to 0.75 mm when the welding speed increases from 1 m/min to 8 m/min. In addition, the average grain area decreases in the region with distance 1.0 mm to 1.5 mm from the top surface at welding speed of 1 m/min. This is because the shape of the weld

pool boundary curves in a way that both the widths of the FZ on the top and bottom surfaces are larger than that in the interior part of the FZ. Thus, the maximum average grain area appears in the interior horizontal x-y plane where the average angles between the growth directions of the columnar grains and the horizontal planes in the 3D domain are minimum.

Fig. 12 (b) shows the variation of average grain area in various longitudinal x-z planes at welding speed of 1 m/min and 8 m/min. The average area drops dramatically from the longitudinal central nearby planes to the interior planes. The difference is that the distance from the longitudinal central plane is significantly larger for welding speed of 1 m/min, which is about 150 μm. Furthermore, the average grain area in the interior longitudinal x-z planes also decreases significantly when the welding speed increases from 1 m/min to 8 m/min.

3.3.6. Quantitative analysis of grain structure in the HAZ

The effect of welding speed on the average size of the equiaxed grains in the HAZ is shown in Fig. 13 (a). The maximum average grain sizes are observed close to the fusion line in all cases. The mean grain sizes decrease with greater distance from the fusion line, which is due to the variation of local thermal cycles. The mean grain sizes decrease with higher welding speed which corresponds to lower heat input. The grain size distributions in the HAZ on the top surface for various welding speeds are shown in Fig. 13 (b). It
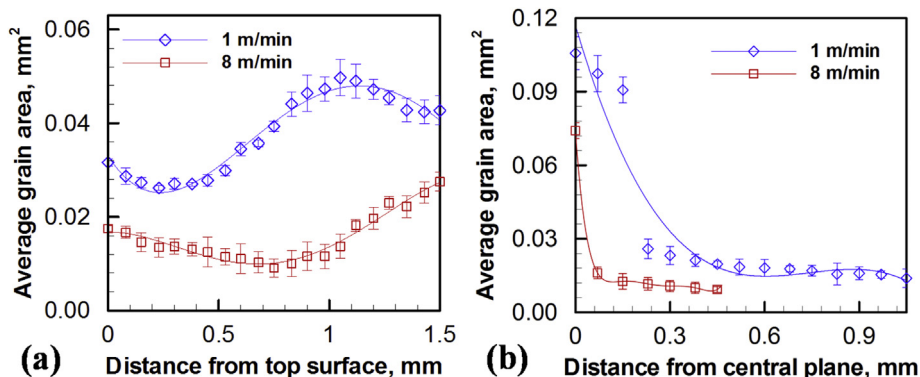

Fig. 12. Comparison of the average grain area in the FZ with various welding speeds. (a) Horizontal x-y planes, (b) longitudinal x-z planes.
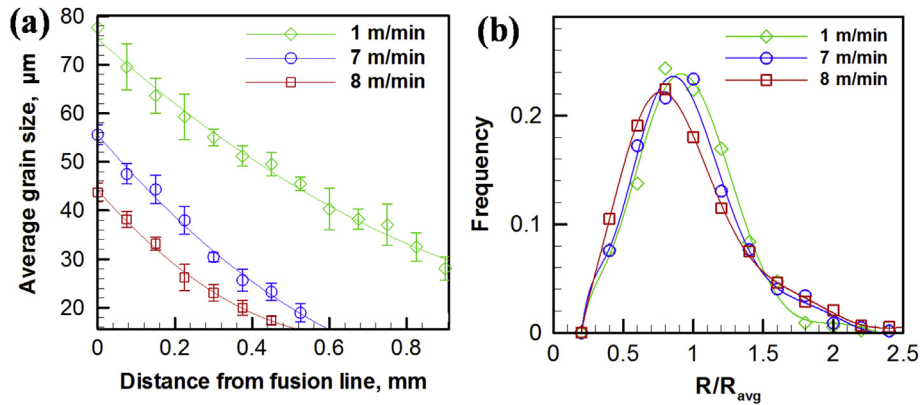
Fig. 13. Comparison of the average size and size distribution of the equiaxed grains in the HAZ with various welding speeds.
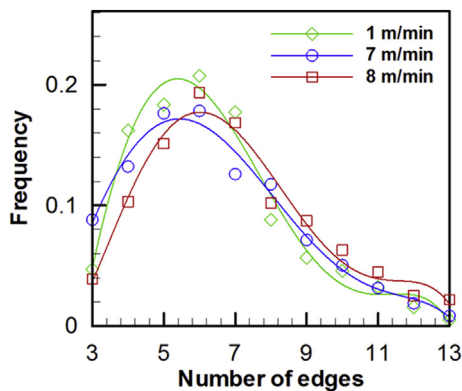

Fig. 14. Comparison of the topological class distribution of the equiaxed grains in the HAZ with various welding speeds.

can be observed that the grain size distributions are all similar despite of different heat inputs and local positions where the measurements are made. The peak frequencies are about 0.22 and the distribution of R/R_{avg} fall in the range between 0.2 and 2.24, which demonstrates that the normalized grain size distributions are independent of the spatial distribution and temporal evolution of the temperature in the HAZ. The reason for this is that any thermal cycles in the HAZ can be visualized as a collection of numerous discreet isothermal steps so that the grain growth under different thermal cycles behaves in a similar manner as that under different isothermal conditions for different times [8].

Fig. 14 shows the topological class distributions in the HAZ for various welding speeds on the top surface. Grains with six edges have highest frequencies and the distributions are characteristics of topological class distributions for isothermal systems. The average edges per grain are approximately equal to six, which is consistent with the general topological rule [9]. The average number of sides of grains in a domain is equal to six and grains with less than six sides tend to shrink and those with more than six sides tend to grow. This is because grain boundary migration occurs if all the grains in a structure are not six sided. The overall result of grain growth is reducing the number of grains, thereby increasing the mean grain size and reducing the total grain boundary energy. The results in Fig. 14 show similar topological features of grains in isothermal systems, which indicates that the topological class distributions in the HAZ are unaffected by the pronounced spatial and temporal variations of the temperature.

4. Conclusions

The evolution of grain structure in both the FZ and the HAZ of the weld has been examined considering the motion, shape and size of the weld pool by a 3D grain growth model using MC calculation. The necessary transient temperature fields during keyhole mode laser welding of copper have been calculated using a well-tested 3D heat transfer and fluid flow model. After validating the model with independent experimental results, the following conclusions are made:

(1) The calculated results showed that the shape of the weld pool varied with welding speed, which further affected the temperate gradients and the maximum heat flow directions at the weld pool boundary. At low welding speed of 1 m/min, the shape of the weld pool surface was elliptical. At higher welding speeds of 7 m/min and 8 m/min, the molten pool surface was significantly elongated. The weld pool trailing edge in the longitudinal central plane was elongated and more inclined with greater welding speed.

(2) The simulated 3D grain structure showed that curved columnar grains growing from the weld pool boundary coexisted with the straight axial columnar grains near the vertical symmetrical plane of the FZ. The columnar grains in the FZ which can be distinctly observed in horizontal sectional planes may appear as equiaxed grains in the transverse and longitudinal vertical planes, which clearly show the potential difficulties in experimental character-ization of grain structures in this and similar systems.

(3) The width and the height of the region composed of axial columnar grains were reduced when the welding speed increased from 1 m/min to 7 m/min and 8 m/min, which was due to the change in maximum heat flow directions at the weld pool boundary.

(4) The size of the columnar grains in the longitudinal sectional planes of the FZ decreased significantly from the central to the off-central planes where the transition from straight axial to curved columnar grains occurs for all the cases. The aspect ratio of the local columnar grains also decreased considerably.

(5) The grain size in the horizontal sectional planes of the FZ initially decreased and then increased with greater distance from the top surface, because of the shape change of the FZ trailing edge. The size of the columnar grains in the FZ decreased with greater welding speed as expected.

(6) The simulated results showed that the grain size in the HAZ decreases with the distance from the fusion line and also

decreases with the increase in welding speed due to weaker thermal cycles. The grain size distributions and topological class distributions in the HAZ were unaffected by welding speeds, which obeyed the normal distribution similar to isothermal systems.

Appendix A. Grain growth model for the HAZ and the FZ

A1.1. Grain growth in the HAZ

The grain growth in the HAZ is simulated using MC technique which is based on Potts' model [24]. The details of the model are available in the literature [8,10,25,26] and only the salient features pertinent to the specific problems in this paper are described here. The grid points are designated in the solid region with 15 μm spacing for the initialization of the simulation process. These grid points are assigned a random orientation number between 1 and q, where q is the total number of possible grain orientations. The initial orientations of each site are represented by random integral numbers between 1 and 48. The adjacent sites have identical orientation number in each individual grain. The grain boundaries locate at the neighbor sites with unlike grain orientations.

The grain boundary energy is determined by defining an interaction between nearest neighbor lattice sites. The local interaction energy E is calculated by the Hamiltonian [30]:

$$E = -J \sum_{j=1}^{n} (\delta S_i S_j - 1) \tag{A.1}$$

where J is a positive constant which sets the scale of the grain boundary energy, δ is Kronecker's delta function, S_i is the orientation at a randomly selected site i, S_j are the orientations of its nearest neighbors, and n is the total number of nearest neighbor sites. Each pair of nearest neighbor contributes J to the total energy when they have unlike orientations.

The kinetics of grain boundary migration are simulated by randomly selecting a site and altering its orientation to one of its nearest neighbor orientations, and judging the system energy variation due to the attempted orientation change. The probability of orientation change is defined as [31]:

$$P = 1 \text{ for } \Delta E \leq 0 \tag{A.2}$$

$$P = e^{-\frac{\Delta E}{k_B T}} \text{ for } \Delta E \geq 0 \tag{A.3}$$

where ΔE is the change of energy due to the change of orientation, k_B is the Boltzmann constant and T is the temperature. Boundary migration, i.e. grain expansion or shrinkage, occurs upon any successful reorientation of a grain to orientations of its nearest neighbors.

The material properties and temperature-time history are considered in the grain growth kinetics using MC technique, which establishes a relation between the MC simulation time (t_{MCS}) and real time through a grain boundary migration model [27]. The expression of the MC time, t_{MCS}, can be described as [32]:

$$t_{MCS} = \left\{ \frac{1}{K_1 \lambda} \left[\frac{4 \gamma A Z V_m^2}{N_a^2 h} e^{\Delta S_a / R} \sum_i \left(\Delta t_i exp \left(-\frac{Q}{R T_i} \right) \right) + L_0^2 \right]^{\frac{1}{2}} - \frac{1}{K_1} \right\}^{\frac{1}{n_1}} \tag{A.4}$$

where λ is the grid spacing, K_1 and n_1 are model constants, γ is the grain boundary energy, A is the accommodation probability, Z is the average number of atoms per unit area at the grain boundary, V_m is the atomic molar volume, N_a is Avagadro's number, h is Planck's constant, ΔS_a is the activation entropy, Q is that activation enthalpy for grain growth, T is the absolute temperature, R is the gas constant, L_0 is the initial average grain size and t is time. Eq. (A.4) indicates that higher values of t_{MCS} are obtained at sites with higher temperature and longer grain growth time.

The site selection probability for all grains is identical due to the random selection of grid points during the update of grain orientation numbers in traditional MC calculations. Actually grains grow faster in regions that experience stronger thermal cycles. The probability p to visit each site is calculated by considering the gradient of t_{MCS} [26]:

$$p = \frac{t_{MCS}}{t_{MCSMAX}} \tag{A.5}$$

where t_{MCS} is the computed MC simulation time at any site and t_{MCSMAX} is the maximum MC simulation time in the entire calculation domain. Eq. (A.5) indicates that locations with higher site probability have higher t_{MCS} and are updated more frequently.

A1.2. Grain growth in the FZ

Columnar grains in the FZ grow epitaxially from the partially melted grains in the HAZ where grain growth also occurs with time. The columnar grains then grow along location dependent directions and speeds. The incremental growth of grains for each time step modifies the local directions and velocities. The solidification direction is parallel to the local maximum temperature gradient, which is normal to the S/L interface, on the trailing side of the molten pool. The temperature gradient G at any location of the S/L interface of the molten pool is calculated by Refs. [20,28,33]:

$$G = \|\nabla T\| = \left\| \frac{\partial T}{\partial x} i + \frac{\partial T}{\partial y} j + \frac{\partial T}{\partial z} k \right\| \tag{A.6}$$

where T is temperature and i, j and k are unit vectors in the welding direction, x, width direction, y and the vertical depth direction, z, respectively. The angle α between the scanning direction and the maximum heat flow direction that the grains follow is calculated by:

$$\cos \alpha = \frac{-\partial T / \partial x}{G} \tag{A.7}$$

The local solidification rate R_{loc} is the speed at the S/L interface on the trailing side of the molten pool moving at steady state, as indicated in Fig. 1. Its value is position dependent and changes from $R_{loc} = 0$ at the maximum weld width to $R_{loc} = R_{max}$ at the centerline on the top surface of the weld. The solidification rate is calculated as:

$$R_{loc} = R_{max} \cdot \cos \alpha \tag{A.8}$$

where R_{max} is the maximum solidification rate which is the same as the scanning speed. The freshly solidified grains thicken in size in the FZ which is simulated using the MC model.

References

[1] R. Rai, J.W. Elmer, T.A. Palmer, T. DebRoy, Heat transfer and fluid flow during keyhole mode laser welding of tantalum, Ti—6Al—4V, 304L stainless steel and vanadium, J. Phys. D Appl. Phys. 40 (18) (2007) 5753—5766.

[2] T. DebRoy, S.A. David, Physical processes in fusion welding, Rev. Mod. Phys. 67 (1) (1995) 85—112.

[3] L.J. Zhang, G.F. Zhang, J. Ning, X.J. Zhang, J.X. Zhang, Microstructure and properties of the laser butt welded 1.5-mm thick T2 copper joint achieved at high welding speed, Mater. Des. 88 (2015) 720—736.

[4] S.A. David, J.M. Vitek, Correlation between solidification parameters and weld microstructures, Int. Mater. Rev. 34 (1) (1989) 213—245.

[5] Y. Kawahito, M. Mizutani, S. Katayama, High quality welding of stainless steel with 10 kW high power fibre laser, Sci. Technol. Weld. Joi 14 (2013) 288—294.

[6] Yousuke Kawahito, Masami Mizutani, Seiji Katayama, Elucidation of high-power fibre laser welding phenomena of stainless steel and effect of factors on weld geometry, J. Phys. D Appl. Phys. 40 (19) (2007) 5854—5859.

[7] J.J. Blecher, C.M. Galbraith, C. Van Vlack, T.A. Palmer, J.M. Fraser, P.J.L. Webster, T. DebRoy, Real time monitoring of laser beam welding keyhole depth by laser interferometry, Sci. Technol. Weld. Join. 19 (7) (2014) 560—564.

[8] S. Mishra, T. DebRoy, Measurements and Monte Carlo simulation of grain growth in the heat-affected zone of Ti—6Al—4V welds, Acta Mater 52 (2004) 1183—1192.

[9] S. Mishra, T. DebRoy, Grain topology in Ti—6Al—4V welds—monte Carlo simulation and experiments, J. Phys. D Appl. Phys. 37 (15) (2004) 2191—2196.

[10] Z. Yang, S. Sista, J.W. Elmer, T. DebRoy, Three dimensional Monte Carlo simulation of grain growth during GTA welding of titanium, Acta Mater. 48 (20) (2000) 4813—4825.

[11] Z. Yang, J.W. Elmer, J. Wong, T. DebRoy, Evolution of titanium arc weldment macro and microstructures - modeling and real time mapping of phases, Weld. J. 79 (2000) 97S—112S.

[12] Wenda Tan, Yung C. Shin, Multi-scale modeling of solidification and micro-structure development in laser keyhole welding process for austenitic stain-less steel, Comput. Mater. Sci. 98 (2015) 446—458.

[13] Shijia Chen, Gildas Guillemot, Charles-André Gandin, 3D coupled cellular automaton (CA)—Finite element (FE) modeling for solidification grain structures in gas tungsten arc welding (GTAW), ISIJ Int. 54 (2) (2014) 401—407.

[14] Shijia Chen, Gildas Guillemot, Charles-André Gandin, Three-dimensional cellular automaton-finite element modeling of solidification grain structures for arc-welding processes, Acta Mater. 115 (2016) 448—467.

[15] H.L. Wei, J.W. Elmer, T. DebRoy, Three-dimensional modeling of grain struc-ture evolution during welding of an aluminum alloy, Acta Mater. 126 (2017) 413—425.

[16] Jie Ning, Lin-Jie Zhang, An Wang, Qing-Lin Bai, Jian-Nan Yang, Jian-Xun Zhang, Effects of double-pass welding and extrusion on properties of fiber laser welded 1.5-mm thick T2 copper joints, J. Mater. Process. Technol. 237 (2016) 75—87.

[17] S. Kou, Welding Metallurgy, second ed., John Wiley & Sons, Hoboken, NJ, 2003.

[18] R. Rai, S.M. Kelly, R.P. Martukanitz, T. DebRoy, A convective heat-transfer model for partial and full penetration keyhole mode laser welding of a structural steel, Metall. Mater. Trans. A 39 (2007) 98—112.

[19] H. Zhao, T. DebRoy, Macroporosity free aluminum alloy weldments through numerical simulation of keyhole mode laser welding, J. Appl. Phys. 93 (12) (2003) 10089—10096.

[20] H.L. Wei, J.W. Elmer, T. DebRoy, Origin of grain orientation during solidifica-tion of an aluminum alloy, Acta Mater. 115 (2016) 123—131.

[21] S.A. David, T. DebRoy, Current issues and problems in welding science, Science 257 (5069) (1992) 497—502.

[22] K. Mundra, T. DebRoy, K.M. Kelkar, Numerical prediction of fluid flow and heat transfer in welding with a moving heat source, Numer. Heat. Tr. A - Appl. 29 (1996) 115—129.

[23] H.L. Wei, J.J. Blecher, T.A. Palmer, T. DebRoy, Fusion zone microstructure and geometry in complete-joint-penetration laser-arc hybrid welding of low-alloy steel, Weld. J. 94 (2015) 135S—144S.

[24] R.B. Potts, Some generalized order-disorder transformations, Proc. Camb. Philos. Soc. 48 (1952) 106—109.

[25] B. Radhakrishnan, T. Zacharia, Simulation of curvature-driven grain growth by using a modified monte carlo algorithm, Metall. Mater. Trans. A 26 (1) (1995) 167—180.

[26] B. Radhakrishnan, T. Zacharia, Monte Carlo simulation of grain boundary pinning in the weld heat-affected zone, Metall. Mater. Trans. A 26 (8) (1995) 2123—2130.

[27] J.H. Gao, R.G. Thompson, Real time-temperature models for Monte Carlo simulations of normal grain growth, Acta Mater 44 (1996) 4565—4570.

[28] H.L. Wei, J. Mazumder, T. DebRoy, Evolution of solidification texture during additive manufacturing, Sci. Rep. 5 (2015). Article number: 16446.

[29] S.R.Koteswara Rao, G. Madhusudhana Reddy, M. Kamaraj, K. Prasad Rao, Grain refinement through arc manipulation techniques in Al—Cu alloy GTA welds, Mater. Sci. Eng. A 404 (1—2) (2005) 227—234.

[30] S. Sista, T. Debroy, Three-dimensional monte carlo simulation of grain growth in zone-refined iron, Metall. Mater. Trans. B 32 (6) (2001) 1195—1201.

[31] M.P. Anderson, D.J. Srolovitz, G.S. Grest, P.S. Sahni, Computer simulation of grain growth—I. Kinetics, Acta Metall. 32 (5) (1984) 783—791.

[32] S. Mishra, T. DebRoy, Non-isothermal grain growth in metals and alloys, Mater. Sci. Technol. 22 (3) (2006) 253—278.

[33] J.J. Blecher, T.A. Palmer, T. DebRoy, Solidification map of a nickel-base alloy, Metall. Mater. Trans. A 45 (4) (2014) 2142—2151.

[34] K. Mills, Recommended Values of Thermophysical Properties for Selected Commercial Alloys, Woodhead Publishing Limited, England, 2002.